NINE

TIME-RESOLVED PHOTON PROPAGATION IN TISSUES

Steven L. Jacques, Lihong Wang, and Andreas H. Hielscher

9.1. INTRODUCTION

Photon movement in a turbid medium such as biological tissue has posed challenging problems due to the strong influence of light scattering at ultraviolet, visible, and near-infrared wavelengths. Photons which escape from a tissue as either reflectance or transmittance may have propagated along many different paths within the tissue. Therefore, it is difficult to interpret the magnitude of photon escape in terms of either tissue absorption or the presence of an internal heterogeneity. The use of measurement techniques which allow time-resolved measurements of photons has offered a new approach toward understanding photon propagation.

The pathlength, L, that a photon has taken within a tissue is proportional to the time, t, a photon spends in the tissue:

$$L = c\,t \tag{9.1}$$

where c is the speed of light in tissue ($c = c_0/n$, where c_0 is the *in vacuo* speed of light and n is the tissue refractive index). For example, a typical tissue with 80% water content has a refractive index of about 1.37 and therefore c equals $(3.0 \times 10^{10}$ cm $s^{-1})/1.37$ or 2.2×10^{10} cm s^{-1}. If the photon escapes 1.0 ns after injection into the tissue, then the pathlength of that photon was ($2.2 \times$

STEVEN L. JACQUES, LIHONG WANG, AND ANDREAS H. HIELSCHER • Laser Biology Research Laboratory, The University of Texas M.D. Anderson Cancer Center, Houston, Texas 77030.

Optical-Thermal Response of Laser-Irradiated Tissue, edited by A. J. Welch and M. J. C. van Gemert, Plenum Press, New York, 1995.

10^{10} cm s^{-1})(10^{-9} s) or 22 cm. In a scattering medium, a 22-cm path can be quite tortuous and the photons primarily escape from the tissue within a couple of cm from the injection point. The photon direction quickly randomizes with respect to its trajectory at injection and continues a random walk within the tissue until it escapes at the tissue surface or is absorbed. Time-resolved photon measurements seek to use the pathlength information implied by the time of escape to specify the optical properties in the volume of tissue traveled by the photons.

In this chapter, the time-resolved movement of photons will be considered.[1] Photon migration can also be discussed in the frequency domain, and a brief presentation of the connection between time-domain and frequency-domain descriptions of photon propagation will be presented. Chapter 10 in this book deals more completely with the topic of frequency-domain measurements. The use of time-resolved photon measurements for spectroscopy and imaging is presented.

9.2. TIME-RESOLVED PHOTON PROPAGATION

This section first considers time-resolved Monte Carlo simulations of photon propagation. Then time-resolved diffusion theory is presented.

9.2.1. Monte Carlo Simulations

Monte Carlo simulations of photon transport treat the photon as a neutral particle whose propagation behaves according to rules of radiative transport. The method ignores wave phenomena such as interference and polarization and concentrates on energy transport. The method derives from a large body of work on neutron transport in the field of nuclear reactors.[2] Chapter 4 of this book discusses Monte Carlo simulations in detail.

As an introduction to time-resolved photon propagation, a time-resolved Monte Carlo simulation (a modified version of MCML—Monte Carlo simulation of Multi-Layered tissues[3]) illustrates the movement of an impulse of photons injected orthogonally into a tissue at its surface at time zero. This example assumes an air/tissue interface and a semi-infinite homogeneous tissue. The tissue has the following optical properties. The absorption coefficient, μ_a, is a low value, 0.1 cm^{-1}, not atypical for soft tissues in the near-infrared spectrum. The scattering coefficient, μ_s, is 100 cm^{-1}, the anisotropy of scattering, g, is 0.9, and the scattering function is the Henyey–Greenstein function (see Chapters 2, 5, and 6). The tissue index of refraction is 1.37.

The distribution of step sizes between sites of photon/tissue interaction (absorption and scattering) is a function of the absorption coefficient μ_a and the scattering coefficient μ_s, as noted in Chapter 4 (Monte Carlo). The probability distribution function $F(\Delta s)$ that the random variable Δs is less than some selected value is given by

$$F(\Delta s) = 1 - \exp(-\mu_t \Delta s) \tag{9.2}$$

where $\mu_t = \mu_a + \mu_s$.

The corresponding density function is

$$p(\Delta s) = \mu_t \exp(-\mu_t \Delta s) \tag{9.3}$$

Based on this density function, photons in a Monte Carlo simulation take variably spaced steps of

$$\Delta s = \frac{-\ln(\text{RND})}{\mu_t} \tag{9.4}$$

where RND is a random number that is uniformly distributed ($0 < \text{RND} \leq 1$). The expected (probability weighted average) value of Δs is $1/\mu_t$ (about 100 μm for the numerical example here). The total pathlength, L, of a photon at any point in time equals the sum of all preceding Δs taken by the photon. Using the weighted photon approach (Chapter 4), the photon's initial weight is set to 1, and after each step the weight attenuates by the factor μ_s/μ_t. This factor, the rate of scattering coefficient to attenuation coefficient, is called the albedo, a. For the selected optical properties used in the sample calculations, $a = 0.999$. After n steps the photon weight equals a^n. After each step, the trajectory of the photon is statistically altered according to the Henyey–Greenstein function.

At each time t, where t is the time requested by the user for mapping the light distribution, the Monte Carlo program propagates a photon until its next step, Δs, will cause the accumulative pathlength, L, to exceed ct. The program truncates the Δs so that the photon position at the exact time t is specified. The current photon weight, a^n, is then deposited in the tissue by incrementing an array element, $U[i, j, t]$, by a^n, where the array refers to a cylindrically symmetric array of elements located at $z = (i + 0.5)\Delta z$ and $r = (j + 0.5)\Delta r$. The array indices i and j are in the following range: $i = 0, 1, \ldots, N_z - 1$ and $j = 0, 1, \ldots, N_r - 1$, where N_z and N_r are the number of grid lines in the z and r directions, respectively. The photon is terminated and a new photon initiated. After N photons have been propagated, the accumulated weight in each array element is normalized in the following manner to yield a descriptor for the instantaneous light energy density distribution, U (in J/cm^3 per J incident energy):

$$U[i, j, t] \leftarrow \frac{U[i, j, t]}{N\,\Delta V[i, j]} \tag{9.5}$$

where $\Delta V[i, j]$ is the volume of the element $[i, j]$ which corresponds to an annulus of radius r and radial width Δr, at depth z with thickness Δz, $\Delta V = 2\pi(i + 0.5)\Delta r^2\Delta z$. Wang and Jacques[3] have considered the connection between discrete array elements and a continuous distribution of light and have concluded analytically that the value $U[i, j, t]$ should be assigned to the radial position that is slightly off the center of each grid element.

In Fig. 9.1a, the contour lines represent the instantaneous energy density distribution in J/cm^3 at 0.46 ps after a 1-mJ impulse incident upon the tissue perpendicularly from the top. At 0.46 ps, L equals 100 μm and on average there has been slightly less than one scattering event (in the simulation, $n = 1$ and $a^n = 0.999$). At 2.3 ps (Fig. 9.1b), L equals 500 μm and most of the impulse has experienced multiple scattering ($a^5 = 0.995$). The light distribution is beginning to spread and scattered light is diffusing back toward the surface. At 46 ps

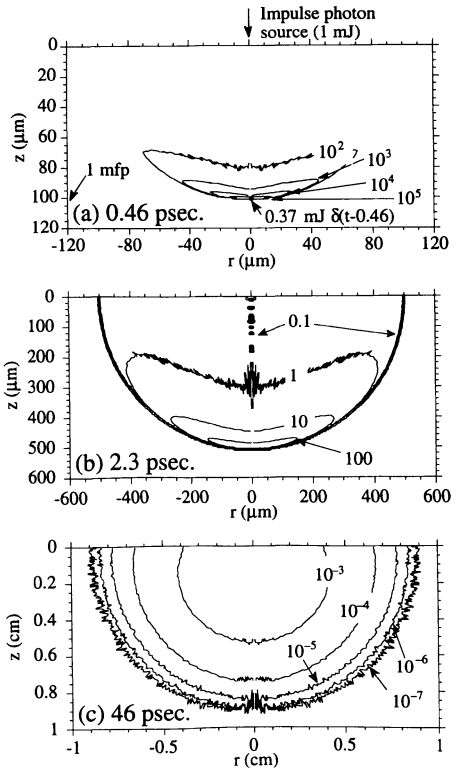

Figure 9.1. The propagation of a 1-mJ laser impulse into tissue (Monte Carlo simulation, $\mu_a = 0.1$ cm^{-1}, $\mu_s = 100$ cm^{-1}, $g = 0.9$, $n = 1.37$). In each figure, a snapshot of the light distribution is depicted as contour curves which indicate iso-density lines in units of J/cm^3. (a) At 0.46 ps, the leading edge of the impulse has traveled 100 μm. The dot at $r = 0$ and $z \approx 100$ μm represents a delta-function that describes the unscattered energy density at 0.46 ps. (b) At 2.3 ps, the leading edge is at 500 μm. (c) At 46 ps, the leading edge is at 1 cm, but is so low in value that it is not shown.

(Fig. 9.1c), L equals 1 cm and on average at least 100 scattering events have been experienced by each surviving photon ($a^{100} = 0.905$). The light distribution has been significantly spread by scattering, and a hemisphere of diffused light is apparent. The noise in the data along the central axis is due to the small bin size, $2\pi r \Delta r \Delta z$, at small r which collects fewer photons.

9.2.2. Diffusion Theory

In the early 1970s, time-resolved diffusion theory was used to describe reflectance of short laser pulses from atmospheric clouds.[4,5] Ishimaru developed a time-dependent diffusion equation that described the transmission of short laser pulses through turbid media.[6] Measurements in experimental solutions have allowed further tests of diffusion theory.[7-11] A lattice model equivalent to diffusion theory has also been used.[12,13]

In an infinite homogeneous medium with no boundary conditions, diffusion theory provides a description for the energy fluence rate, $\phi(\boldsymbol{r}, t)$ (W/m^2), which satisfies the diffusion equation[10,14]:

$$\frac{1}{c}\frac{d}{dt}\phi(\boldsymbol{r}, t) - D\nabla^2\phi(\boldsymbol{r}, t) + \mu_a\phi(\boldsymbol{r}, t) = S(\boldsymbol{r}, t) \tag{9.6}$$

where D is the diffusion constant:

$$D = \frac{1}{3[\mu_a + \mu_s(1 - g)]} \tag{9.7}$$

and where $S(\boldsymbol{r}, t)$ is the source in W/m^3. The solution in response to an impulse $\delta(0,0)$ is given by

$$\phi(r, t) = c(4\pi Dct)^{-3/2}\exp\left(-\frac{r^2}{4Dct} - \mu_a ct\right) \tag{9.8}$$

such that

$$\int_0^{ct}\int_0^{t} \mu_a\phi(r, t)dt\, 4\pi r^2 dr = 1 - \exp(-\mu_a ct) \tag{9.9}$$

which expresses conservation of energy. The rate of energy deposition, $\mu_a\phi$ (J m^{-3} s^{-1}), integrated over the spatial extent that light can travel, ct, and integrated over the time of travel, t, yields the amount of energy deposited by absorption, $1 - \exp(-\mu_a ct)$. This diffusion theory solution becomes relatively accurate at times $t >> 1/[(\mu_a + \mu_s')\, c]$, after many interaction events have occurred.[6,15]

9.3. EQUIVALENCE IN THE FREQUENCY DOMAIN

The description of photon migration in the time domain is complemented by the equivalent description in the frequency domain. Rather than a pulsed light source, a sinusoidally amplitude-modulated source with DC amplitude ϕ_0 and AC amplitude ϕ_1 at a frequency, f, is used to launch photons into the tissue. In this way, photon density waves are generated which propagate in the tissue with fast decaying DC and AC amplitudes. The propagation of the photon density wave initiated by a point source within an infinite homogeneous medium is described by the net fluence rate, ϕ, in W/m^2 at a position r and time t[16]:

$$\begin{aligned}\phi(r,t) &= \mathrm{DC}(r) + \mathrm{AC}(r)\exp[i(k_i r - \omega t)] \\ &= \phi_0 \frac{\exp(-r/\delta)}{r} + \phi_1 \frac{\exp(-k_r r)}{r}\exp[i(k_i r - \omega t)]\end{aligned} \tag{9.10}$$

where $\omega = 2\pi f$ and:

$$\delta = \{3\mu_a[\mu_a + \mu_s(1-g)]\}^{-1/2} \tag{9.11}$$

$$k_r = \frac{1}{\delta}\left[\frac{[1 + (2\pi f/\mu_a c)^2]^{1/2} + 1}{2}\right]^{1/2} \equiv \frac{c_r}{\delta} \tag{9.12}$$

$$k_i = \frac{1}{\delta}\left[\frac{[1 + (2\pi f/\mu_a c)^2]^{1/2} - 1}{2}\right]^{1/2} \equiv \frac{c_i}{\delta} \tag{9.13}$$

The demodulation, M, is defined by the ratio of the AC part and DC part at a distance r from the source, divided by the ratio of the AC part ϕ_1 and DC part ϕ_0 of the source itself. The phase, θ, and demodulation, M, of the photon density wave can be expressed as

$$\theta = k_i r = \frac{c_i}{\delta} r \tag{9.14}$$

and

$$M = \frac{\mathrm{AC}(r)/\mathrm{DC}(r)}{\phi_1/\phi_0} = \frac{\exp(-k_r r)}{\exp(-r/\delta)} = \exp\left[-\frac{r}{\delta}(c_r - 1)\right] \tag{9.15}$$

The velocity, v_p, and wavelength, λ_m, of the photon density wave are given by

$$v_p = \omega/k_i = \frac{2\pi f}{c_i}\delta \tag{9.16}$$

and

$$\lambda_m = v_p/f = \frac{2\pi}{c_i}\delta \tag{9.17}$$

All four parameters are functions of the medium optical properties and the modulation frequency. A typical photon density wave modulated at 200 MHz in

a medium with given optical properties ($\mu_a = 0.1\ \text{cm}^{-1}$, $\mu_s\,(1\text{-}g) = 10\ \text{cm}^{-1}$, $n = 1.37$) will have a 9.2-cm wavelength and a wave velocity equal to 6.2% the speed of light. At 1 cm from the source, the phase equals 0.159 radian (9.103 degrees) and the demodulation equals 0.979. In experiments one generally measures the phase θ and the demodulation M.

The formulas for the phase shift θ and demodulation factor M are different only in form from those in Chapter 10; mathematically they are equivalent. The following two relations are used to convert the two types of formulas[17]:

$$\left[\frac{1 + [1 + (\omega/\mu_a c)^2]^{-1/2}}{2}\right]^{1/2} = \cos\left[\frac{1}{2}\tan^{-1}(\omega/\mu_a c)\right] \tag{9.18}$$

$$\left[\frac{1 - [1 + (\omega/\mu_a c)^2]^{-1/2}}{2}\right]^{1/2} = \sin\left[\frac{1}{2}\tan^{-1}(\omega/\mu_a c)\right] \tag{9.19}$$

Roots can be computed much faster than trigonometric functions. Thus the root-notation seems to be advantageous if applied in fitting algorithms to determine optical properties from θ and M measurements.

In practice the intensity modulation of the light source is achieved by the use of electro- or acousto-optical modulators, which provide modulations up to ~300 MHz.[18] Higher modulation frequencies can be reached if laser diodes are used. Their intensity can be modulated up to several GHz by directly modulating the drive current.[19] It is interesting to note that pulsed light source can also be used for measurements in the frequency domain. For example, the output of a free-running mode-locked laser with a repetition rate of 70 MHz contains frequency components which are multiples of 70 MHz. The phase shift and demodulation of these frequency components can be measured.[20] Chapter 10 discusses frequency-domain measurements in more detail. In the remainder of this section, we explain the relationship between time-domain and frequency domain measurements.

9.3.1. Discrete Fourier Transform

A signal $h(t)$ in the time domain is related to its counterpart $H(f)$ in the frequency domain by the Fourier transform

$$H(f) = \int_{-\infty}^{\infty} h(t)\exp(i\,2\pi\,ft)\,dt \tag{9.20}$$

However, in practice one does not have information about $h(t)$ for all times from $-\infty$ to $+\infty$. A signal is generally acquired as consecutive data points, h_k, at times t_k, separated by Δt, such that $t_k = k\Delta t$. If N data points are acquired,

rather than calculating the integral in Eq. (9.20), one computes the *discrete* Fourier transform H_n, which is given by[21]

$$H_n = \sum_{k=0}^{N-1} h_k \exp\left(\frac{2\pi i k n}{N}\right) \tag{9.21}$$

In general the discrete Fourier transform maps N complex numbers, h_k, which in this case is a time series of real numbers, into N complex numbers H_n. The relation between the discrete Fourier transform of a set of numbers and the continuous Fourier transform when they are viewed as samples of a continuous function sampled at an interval Δt can be written as

$$\begin{aligned} H(f_n) &= \int_{-\infty}^{\infty} h(t) \exp(i\, 2\pi f_n t)\, dt \\ &\approx \sum_{k=0}^{N-1} h_k \exp(i\, 2\pi f_n t_k)\Delta t \\ &= \Delta t \sum_{k=0}^{N-1} h_k \exp\left(\frac{i\, 2\pi k n}{N}\right) \\ &= \Delta t\, H_n \end{aligned} \tag{9.22}$$

where the nth frequency, f_n, equals $n/N\Delta t$ (n = −N/2 to N/2). The spacing in the frequency domain is

$$\Delta f = \frac{1}{N\Delta t} \tag{9.23}$$

while the maximum frequency $f_{\max}$ is given by the "Nyquist frequency":

$$f_{\max} = \frac{1}{2\Delta t} \tag{9.24}$$

The accuracy of the approximation made in Eq. (9.22) [$H(f_n) \approx \Delta t H_n$] depends on two restrictions. First, the signal $h(t)$ has to be confined in time. That means before a certain time t_1 and after a certain time $t_2 > t_1$ the signal $h(t)$ must be negligible. If $h(t)$ is the response to an instantaneous point source of light, the energy fluence rate $\phi(r, t)$, is often approximately confined to the interval 0–3 ns. There is no signal before time zero, $h(t < 0) = 0$, and negligible signal for later times, $t > 3$ns, when the signal has decayed by a factor typically on the order of 10^{-5} (see Fig. 9.2a). Thus $h(t)$ values before 0 and after 3 ns contribute negligibly to the sum given in Eq. (9.21). Second, Δt has

to be chosen small enough, so that f_{max} is larger than the maximal frequency contributing to the signal. Otherwise so-called "aliasing" occurs, which is the back folding of frequencies above f_{max} into the spectrum below f_{max}. A Δt of 20 ps which yields $f_{max} = 25$ GHz has been found to be sufficient for most tissues.

If one wants to have a smaller spacing, Δf, in between points in the frequency domain, than allowed by Eq. (9.23), one can simply append zeros to the measured discrete signal $h(t)$. If one appends M values of $h(t)$ equal to zero to the data list of $[t, h(t)]$, in other words, $h(t) = 0$ for $k > N-1$, the sum of Eq. (9.21) is not changed:

$$H_n = \sum_{k=0}^{N-1} h_k \exp\left(\frac{2\pi ikn}{N}\right) = \sum_{k=0}^{N+M-1} h_k \exp\left(\frac{2\pi ikn}{N+M}\right) \tag{9.25}$$

However, now H_n can be evaluated for $n = 0$ to $N + M - 1$ to yield $N + M$ points in the frequency domain, rather than only N points. Since f_{max} depends only on Δt [see Eq. (9.24)], the additional zeros just lead to a smaller spacing in the frequency domain, which is now given by

$$\Delta f = \frac{1}{(N + M)\Delta t} \tag{9.26}$$

The accuracy of the transform is not affected. The additional points in the frequency domain, due to adding zeros in the time domain, may be viewed as interpolations between the "real" points which allow for a smoother curve when plotting the data. This technique is called zero-padding or zero-filling.[21]

Computing the discrete Fourier transform as given in Eq. (9.21) can be very time-consuming. A special algorithm, which is well known as the fast Fourier transform (FFT), provides a way to calculate the sum given in Eq. (9.21) very rapidly, without changing the result. In order to perform the FFT, the number of data points N has to equal an integer power of 2. In the following example, a published FFT algorithm[21] has been used to convert a list of $[t, h(t)]$ values into a list of $[\mathrm{Re}(H(f_n)), \mathrm{Im}(H(f_n))]$, which are the real and imaginary components of $H(f_n)$.

Once $\mathrm{Re}(H(f_n))$ and $\mathrm{Im}(H(f_n))$ have been calculated, the phase shift, θ, and the demodulation, M, for a photon density wave can be determined:

$$\theta = \arctan\left(\frac{\mathrm{Im}\,(H(f_n))}{\mathrm{Re}\,(H(f_n))}\right) \tag{9.27}$$

and

$$M = \sqrt{\frac{\mathrm{Re}^2\,(H(f_n)) + \mathrm{Im}^2\,(H(f_n))}{\mathrm{Re}^2\,(H(0))}} \tag{9.28}$$

9.3.2. Comparison of Time Domain and Frequency Domain

Figure 9.2 shows a typical time-resolved reflectance measurement (Monte Carlo simulation). An impulse of laser radiation is delivered orthogonally to a tissue surface at $r = 0$ (tissue optical properties: $\mu_a = 0.1\ \text{cm}^{-1}$, $\mu_s = 100\ \text{cm}^{-1}$, $g = 0.90$, $n = 1.37$). A 1-mm-diameter collection fiber is placed 1 cm from the origin to collect reflected light. Figure 9.2a shows the time-resolved reflectance, $R(r, t)$, per unit area per unit time in units of $\text{mm}^{-2}\text{ns}^{-1}$.

Figure 9.2b shows the corresponding frequency-domain description of the Fourier-transformed time-resolved data expressed as phase and modulation. The phase increases with frequency. The modulation decreases with frequency. Such frequency-domain behavior is expected, as discussed in Chapter 10.

9.4. SPECTROSCOPY

The motivation for time-resolved measurements as applied to absorption spectroscopy is to specify the absorption coefficient, μ_a, of a medium despite light scattering. In this section, two aspects of time-resolved spectroscopy are considered: (1) a homogeneous tissue, and (2) a heterogeneous tissue.

9.4.1. Homogeneous Tissue

Consider the local time-resolved reflectance, $R(r, t)$, and the total time-resolved reflectance, $R(t)$, from a tissue. Patterson *et al.*[10] considered the behavior of these reflectance measurements when made at the mismatched air/tissue surface boundary of a semi-infinite medium using diffusion theory. The resulting reflectance functions are given by

$$R(r, t) = (4\pi Dc)^{-3/2} (\mu_s')^{-1} t^{-5/2} \exp\left[- \frac{r^2 + (\mu_s')^{-2}}{4Dct} \right] \exp(-\mu_a ct) \quad (9.29)$$

and

$$R(t) = \int_0^\infty R(r, t)\, 2\pi r\, dr = (4\pi Dc)^{-1/2} (\mu_s')^{-1} t^{-3/2} \exp\left[- \frac{(\mu_s')^{-2}}{4Dct} \right] \exp(-\mu_a ct) \quad (9.30)$$

where D is the optical diffusion constant, $[3(\mu_a + \mu_s')]^{-1}$. The $\mu_a c$ term indicates the absorption of the light and the other terms are due to the early spread-

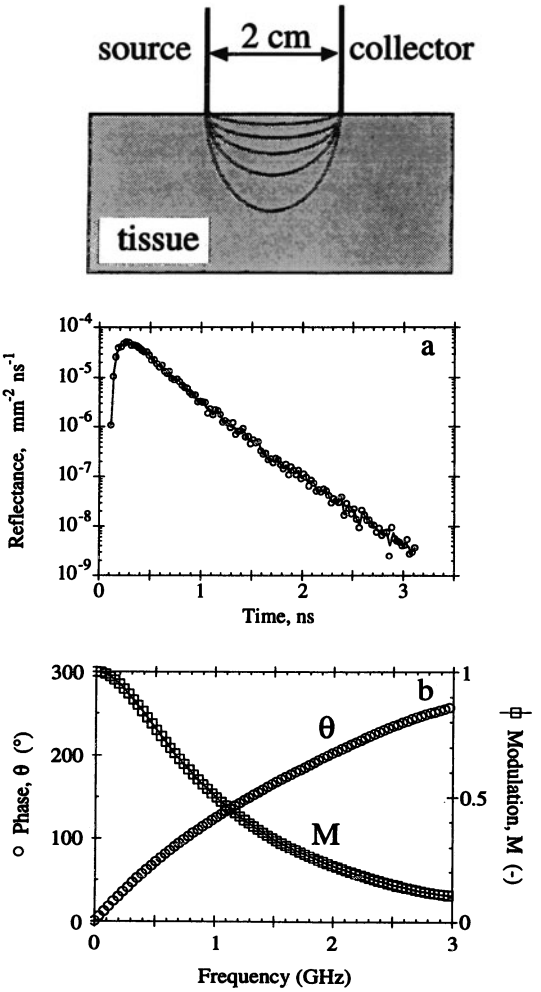

Figure 9.2. Time-domain and frequency-domain descriptions of photon propagation. The model is a source and collector fiber separated by 2 cm. The tissue optical properties are $\mu_a = 0.1$ cm^{-1}, $\mu_s = 100$ cm^{-1}, $g = 0.9$, n = 1.37. (a) Time-resolved local reflectance, $R(r, t)$, based on Monte Carlo simulation. (b) Phase, θ, and demodulation, M, of photon density waves in frequency domain, obtained by Fourier transform of data in (a).

ing of the light in the tissue. The $t^{-5/2}$ and $t^{-3/2}$ terms dominate the early dynamics of the reflectance signals. The negative time derivative of the logarithm of the reflectances yields expressions which are proportional to the absorption coefficient:

$$-\frac{d\ln[R(r,t)]}{dt} = \mu_a c + \frac{5}{2t} - \frac{r^2 + (\mu_s')^{-2}}{4Dct^2} \approx \mu_a c \qquad \text{as } t \to \infty \tag{9.31}$$

$$-\frac{d\ln[R(t)]}{dt} = \mu_a c + \frac{3}{2t} - \frac{(\mu_s')^{-2}}{4Dct^2} \approx \mu_a c \qquad \text{as } t \to \infty \tag{9.32}$$

In principle, $-d\ln[R]/dt$ approaches a straight line with a negative slope equal to $\mu_a c$ at large t. In practice, the second terms should be included while the third terms may be neglected. For example, when $\mu_a = 0.1\ \text{cm}^{-1}$ and $\mu_s' = 10\ \text{cm}^{-1}$, the second terms are comparable with the first terms until several nanoseconds, that is, about the same as the data acquisition time (see Fig. 9.2a). However, the third terms become negligible after only several hundred picoseconds. Therefore, the absorption coefficient can be estimated by

$$\mu_a \approx -\frac{1}{c}\left\{\frac{d\ln[R(r,t)]}{dt} + \frac{5}{2t}\right\} \qquad \text{for large } t \tag{9.33}$$

$$\mu_a \approx -\frac{1}{c}\left\{\frac{d\ln[R(t)]}{dt} + \frac{3}{2t}\right\} \qquad \text{for large } t \tag{9.34}$$

Jacques[22] considered the time delay before diffusion theory agrees with time-resolved Monte Carlo simulations. The key question is how rapidly will the $t^{-3/2}$ or $t^{-5/2}$ terms of Eqs. (9.29) and (9.30) decay so that the dynamics are dominated by μ_a. Figure 9.3 illustrates the problem.

In Fig. 9.3,[23] an experimental measurement of $R(r, t)$ for a semi-infinite medium and $\phi(r, t)$ for an infinite medium were made using a pair of optical fibers which were adjoined with only 150-μm separation. One fiber delivered approximately 4-ps pulses from a mode-locked laser (633 nm, Ultrafast Kinetics Laboratory, Univ. of Texas at Austin). The second fiber collected light for detection by a streak camera (Hamamatsu Photonics). System dispersion broadened the impulse response to about 25 ps. The two-fiber catheter was placed either at the surface of a phantom scattering medium (Intralipid) or within the volume of the medium. The surface measurement involved a boundary and behaved as an $R(r, t)$ measurement with a $t^{-5/2}$ behavior. In contrast, the intravolume measurement had no boundary and the source and collector fibers were very close together at approximately the origin of a one-dimensional problem in spherical coordinates, similar to Eq. (9.8) which predicts $t^{-3/2}$ behavior for r close to zero. In both cases, several hundred ps had to pass before the μ_a began to exert its influence on the signal's behavior. In Fig. 9.3, theoretical curves are drawn for a series of μ_a values to illustrate the time delay before μ_a exerts its influence. Curves for $\mu_a = 0.001$, 0.01, and $0.02\ \text{cm}^{-1}$ are

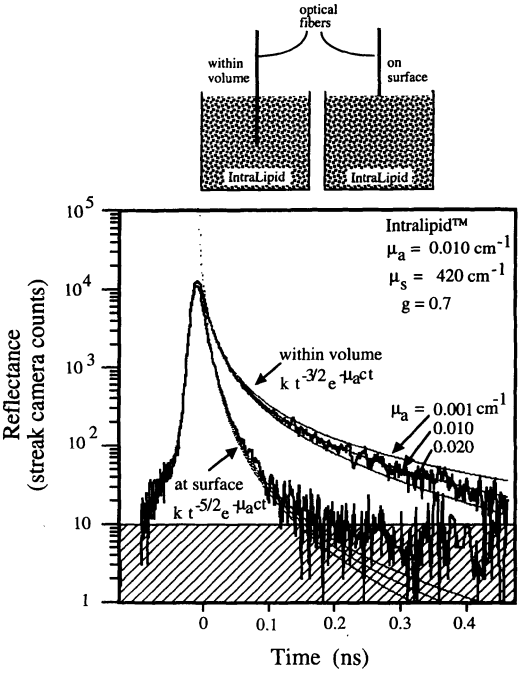

Figure 9.3. Experimental example of time-resolved reflectance.[23] A pair of adjoined optical fibers, one source and one collector, were placed either at the surface or within a volume of Intralipid. A 633-nm mode-locked laser delivered 4-ps pulses and the collected photons were detected by a streak camera. The surface measurement decayed as $t^{-5/2}\exp(-\mu_a ct)$, typical of local reflectance $R(r, t)$. The intravolume measurement decayed as $t^{-3/2}\exp(-\mu_a ct)$, typical of total reflectance $R(t)$. The presence of a boundary condition significantly affected the rate at which the absorption term, $\exp(-\mu_a ct)$, dominated the behavior.

shown, and several hundred ps are required before the curves separate sufficiently to discriminate μ_a. For the surface measurement, the signal falls into the noise before absorption can exert sufficient effect for reliable measurement of μ_a. For the volume measurement, the signal remains above the noise and the μ_a can be deduced to be about 0.01 cm^{-1}. This experiment emphasizes the important role that scattering and boundary conditions can play in the early time-resolved reflectance. At long times the behavior becomes dominated by μ_a.

The relation between the reduced scattering coefficient, $\mu_s(1-g)$, and the time, $t_{\max}$, at which the peak in time-resolved reflectance occurs at a collection site distant from the source can be specified. Patterson *et al.*[10] pointed out that $\ln[R(r, t)]$ reaches a peak value at the time $t_{\max}$ which is determined by

$$\mu_a c + \frac{5}{2t_{\max}} - \frac{r^2 + (\mu_s')^{-2}}{4Dct_{\max}^2} = 0 \tag{9.35}$$

when $r >> 1/\mu_s'$. Equation 9.35 can be stated as

$$\mu_s (1-g) = \frac{1}{3r^2}\left(4\mu_a c^2 t_{max}^2 + 10 c t_{max} \right) - \mu_a \tag{9.36}$$

Figure 9.4 illustrates the relation between r and t_{max}. An impulse of light is injected at the origin at time zero and $R(r, t)$ is collected at r equal to 0.2, 1, 2, and 3 cm. The circles indicate data from a Monte Carlo simulation and the

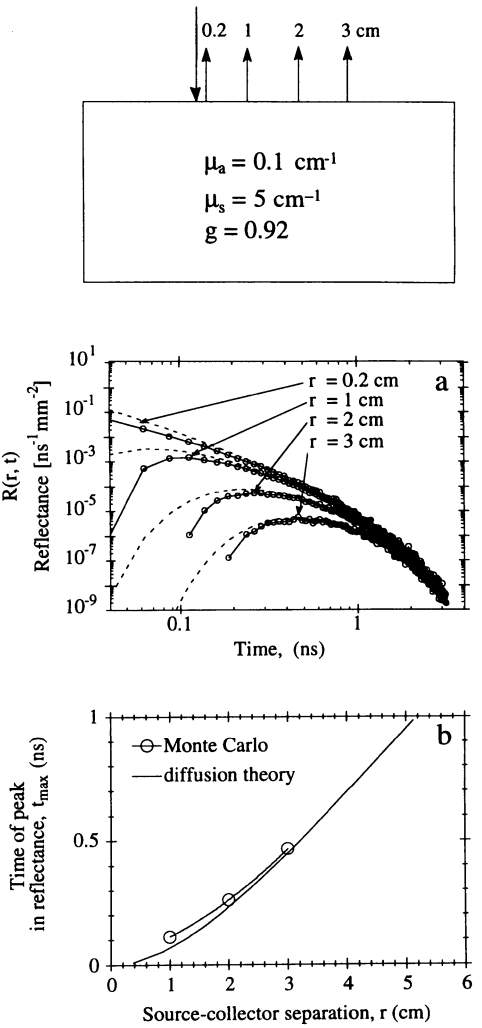

Figure 9.4. Time-of-peak indicates the effective scattering, $\mu_s(1-g)$. A Monte Carlo simulation of time-resolved reflectance at different distances from the source: r = 0.2, 1, 2, and 3 cm. (a) Time-resolved $R(r,t)$. Arrows indicate peaks, t_{max}. (b) Relation between t_{max} and r. Dashed line indicates diffusion theory description, Eq. (9.29). Monte Carlo data approaches dashed line at large r.

dashed lines indicate the predictions of diffusion theory [$\mu_a = 0.1\ \text{cm}^{-1}$, $\mu_s(1-g) = 5\ \text{cm}^{-1}$, $g = 0.92$]. The arrows in Fig. 9.4a indicate the peaks $R(r, t_{\max})$. In Fig. 9.4b, $t_{\max}$ is plotted versus r. The dashed line indicates the diffusion theory relation of Eq. (9.36). The Monte Carlo data approach diffusion theory as r increases.

9.4.2. Example

The absorption coefficient equals the sum of all the contributions to absorption by chromophores in the tissue:

$$\mu_a = \ln(10) \sum_i \varepsilon_i C_i \tag{9.37}$$

where ε_i and C_i are the extinction coefficient and concentration, respectively, for the ith chromophore in the tissue, defined such that the product εC is in units of cm^{-1} and transmission through a pathlength L equals $10^{(-\varepsilon CL)}$. Since different chromophores have different absorption spectra (assume these are known), linear analysis of a complex spectrum can be resolved into the component spectra due to each chromophore to yield the concentration, C_i, of each chromophore.

One example is the deduction of the concentration of oxyhemoglobin and deoxyhemoglobin in tissue based on measurements at 3 properly chosen wavelengths. Figure 9.5a plots the extinction coefficients for oxyhemoglobin and deoxyhemoglobin as functions of wavelength, i.e., $\varepsilon_{ox}(\lambda)$ and $\varepsilon_{de}(\lambda)$, respectively.[24] Three wavelengths (λ_1, λ_2, λ_3) are indicated by arrows where measurements of diffuse reflectance are made. Figure 9.5b illustrates typical time-resolved reflectances simulated with diffusion theory. In practice, the three $R(r, t)$ measurements specify three wavelength-dependent absorption coefficients. Assuming the absorption coefficient of the background tissue (μ_{abg}) is wavelength-independent in the wavelength range λ_1 to λ_3, one can solve the following equations for the concentrations of oxyhemoglobin and deoxyhemoglobin, C_{ox} and C_{de}, and the background absorption coefficient, μ_{abg}:

$$\begin{aligned}
\mu_a(\lambda_1) &= \ln(10)\,[\varepsilon_{ox}(\lambda_1)\,C_{ox} + \varepsilon_{de}(\lambda_1)\,C_{de}] + \mu_{abg} \\
\mu_a(\lambda_2) &= \ln(10)\,[\varepsilon_{ox}(\lambda_2)\,C_{ox} + \varepsilon_{de}(\lambda_2)\,C_{de}] + \mu_{abg} \\
\mu_a(\lambda_3) &= \ln(10)\,[\varepsilon_{ox}(\lambda_3)\,C_{ox} + \varepsilon_{de}(\lambda_3)\,C_{de}] + \mu_{abg}
\end{aligned} \tag{9.38}$$

Such measurements are currently being developed for clinical application.[25–27]

Another aspect of spectroscopy is specification of a tissue's scattering properties, which departs from classical absorption spectroscopy but is becom-

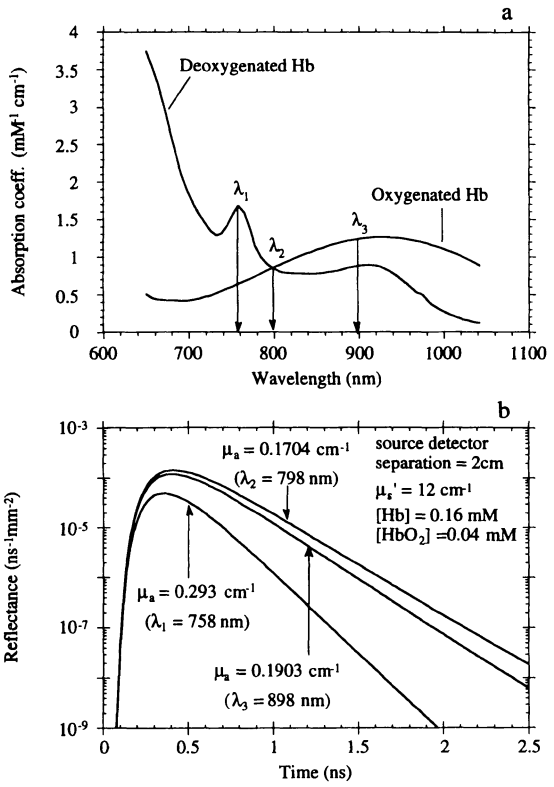

Figure 9.5. (a) Near-IR absorption spectra for oxyhemoglobin and deoxyhemoglobin expressed as the extinction coefficient, ε, in $mM^{-1}cm^{-1}$.[24] Arrows indicate three typical wavelengths used for measurements to specify the blood content and oxygenation status of the tissue. (b) Local time-resolved diffuse reflectance for bloodless and blood-filled tissue (simulated by diffusion theory). The tissue scattering coefficient, $\mu_s(1-g)$, is assumed to be 12 cm^{-1} and wavelength-independent in this spectral range. The background absorption of the bloodless tissue is assumed to be wavelength-independent in this spectral region: $\mu_{abg} = 0.03\ cm^{-1}$, and the bloodless curve is shown for reference. The other curves show the $R(r, t)$ for a blood-filled tissue at the three wavelengths indicated in (a). The blood-filled tissue has a hemoglobin (HGb) concentration of 0.20 mM, 20% oxyhemoglobin and 80% deoxyhemoglobin. The slope of each curve indicates μ_a, where $\mu_a = \mu_{abg} + \ln(10)\varepsilon_{ox}C_{ox} + \ln(10)\varepsilon_{de}C_{de}$ [see Eq. 9.38)]. By measuring the three slopes for the three wavelengths, the three unknowns [μ_{abg}, blood concentration ($C_{ox} + C_{de}$), and oxygenation status $C_{ox}/(C_{ox} + C_{de})$] are specified.

ing very important as a means of characterizing tissues. Abnormal tissues often appear to display different scattering properties and this type of information is likely to become increasingly pertinent to medical diagnostics.

9.4.3. Heterogeneous Medium

Time-resolved measurements provide a unique approach toward probing a heterogeneous medium where a distinct object or tissue layer is embedded within a homogeneous medium. The time of photon escape is related to the pathlength of the photon. Therefore, by observing the early versus late behavior of photon escape one can distinguish the presence and, to some extent, the optical properties of a buried object or layer. Initially, the photons propagate in the homogeneous medium before they encounter a buried object. Only after some time delay do the first photons encounter the object. Finally, the ensemble of photons which have encountered and interacted with the object must propagate back to the collector before the presence of the object can be detected. Therefore, the initial measurement will represent photons that have not encountered the object and have propagated directly to the detector. This measurement will suggest a homogeneous medium but, after some time delay, the signal will depart from the expected behavior for a homogeneous medium. That time delay provides information about the depth of the object or layer. The magnitude of the deviation can indicate the average absorption coefficient of the heterogeneous medium.

A Monte Carlo simulation of this concept is illustrated in Fig. 9.6. A scattering medium ($\mu_a = 0\ \text{cm}^{-1}$, $\mu_s(1-g) = 5\ \text{cm}^{-1}$, $g = 0.92$, $n = 1.37$) has a buried layer with a higher absorption coefficient ($\mu_a = 0.1\ \text{cm}^{-1}$, same scattering). The depth of the absorbing layer is either ∞, 6 mm, 3 mm, or 0 as indicated in the figure. The source–collector separation is 1 cm. Figure 9.6a plots $R(r, t)$ versus time on a log-linear plot. The 6-mm curve deviates from the ∞ curve at about 240 ps, indicated by a large open circle and X arrow. The 3-mm curve deviates from the ∞ curve at about 70 ps (see Y arrow), although this point has poor resolution in this simulation. Figure 9.6b plots the delay time, t_d, when deviation from the homogeneous curve occurs versus the depth, z, of the buried layer. The dashed curve described by $z^2 = Dct_d$ is a tentative description for predicting the depth of a buried layer from the delay time t_d, where D is the diffusion constant for the nonabsorbing layer.

9.5. IMAGING

The motivations for optical imaging are (1) to avoid ionizing radiation such as X rays, (2) to detect tumors with good contrast, and (3) to avoid expen-

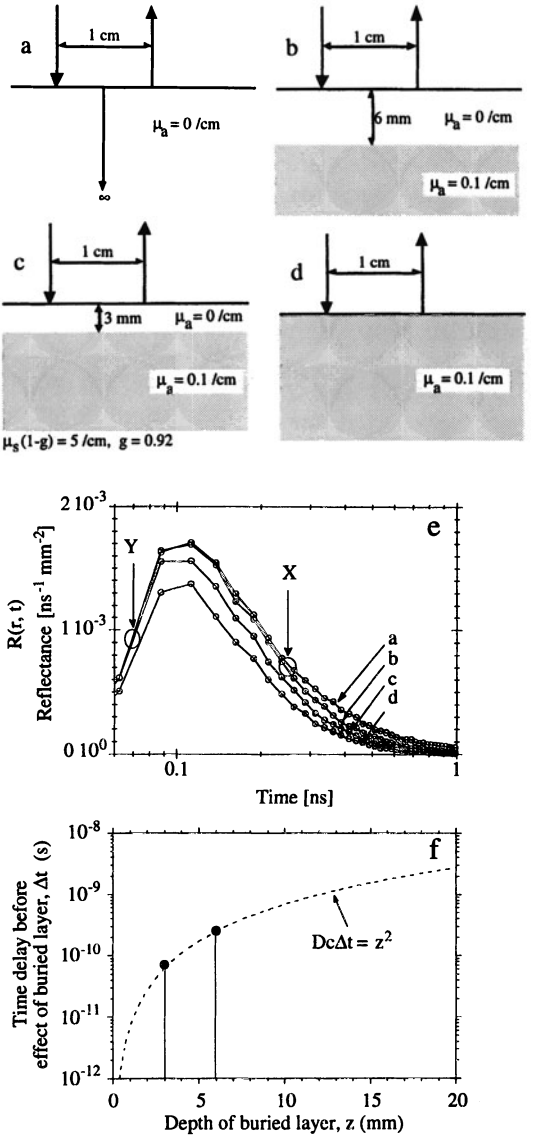

Figure 9.6. Detection of a buried layer. (a–d) A source and collection fiber are separated by 1 cm. The medium has no absorption and is scattering ($\mu_a = 0$ cm^{-1}, $\mu_s(1-g) = 5$ cm^{-1}). A buried layer has the same scattering but some absorption ($\mu_a = 0.1$ cm^{-1}), and the absorbing layer is located at $z = \infty$, 6, 3, or 0 mm. The time required for an ensemble of photons to propagate to and interact with the buried layer and then return to the surface constitutes a time delay, Δt, before the $R(r,t)$ curves deviate from the control curve *a*. (e) Curve b for the 6-mm-deep absorbing layer deviates from curve a at about 240 ps. Curve c for the 3-mm-deep layer deviates at ~70 ps. (f) The relation between the delay before deviation, Δt, and the depth of the buried layer, z, is shown. The dashed line is $Dc\Delta t = z^2$, where $D = 1/(3\,\mu_s') = 1/15$ cm.

sive imaging such as magnetic resonance imaging (MRI) or positron emission tomography (PET). Although the quality of the images may be very limited, as a low-cost initial screening tool optical imaging could earn a place in medicine, if it works.

Two approaches toward imaging are under investigation by many groups. (1) Transmittance-mode imaging uses the few early transmitted photons which cast shadows of internal objects within the tissue and rejects the many late photons which are highly scattered and obscure the shadow image. (2) Reflectance-mode imaging uses the few late reflected photons which have probed deeper tissue layers and rejects the many early photons which have probed only the superficial tissue layers. Section 9.4.3 discussed a situation similar to reflectance-mode imaging. This section will discuss transmittance-mode imaging.

One of the research directions is to use transmitted ballistic photon or quasi-ballistic photon detection. Ballistic photons are those passing through the tissue without scattering, and quasi-ballistic photons are those with a small number of scatterings but only a slight deflection from their original trajectory. Due to the highly forward-directed nature of scattering in tissue (anisotropy factor greater than 0.9), after a small number of scatterings the photons may still carry some imaging information about the optical properties along the ballistic path with a certain amount of resolution.

For example, one scenario for optical imaging proposes to use time-resolved transmission measurements to image tumors in soft tissues such as the breast. Analogous to X-ray tomography, the transmission of photons could be measured at many angles around the breast and the data analyzed by tomographic algorithms to yield a mapping of fluctuations in optical density (hopefully tumors). By time gating the detector so that only the early quasi-ballistic photons are collected, the detector avoids being "blinded" by the large number of scattered photons which eventually transmit through the tissue but arrive at later times due to their longer pathlengths. Experimentally, time gating has been accomplished using streak camera, nonlinear crystals, and Kerr gates.

In this section two aspects of the problem are considered: (1) How many scattering events must occur to obtain one detectable transmitted photon given a reasonable incident number of photons? The problem is addressed by considering a simplified ideal condition where scattering does not alter the path of a photon ($g = 1$). Although an ideal case, the treatment illustrates the minimum number of scattering events that must occur. (2) How will anisotropy influence the imaging capability of the transmitted photons? Monte Carlo simulations will illustrate how the anisotropy affects the propagation of quasi-ballistic photons.

9.5.1. Quasi-Ballistic Photons

Ballistic photon detection is not possible for the thick biological tissues of interest such as the breast, brain, or a muscle mass. Consider a tissue that is 5

cm thick with a scattering coefficient, μ_s, of 100 cm^{-1} (absorption is much lower than scattering and shall be neglected). Beer's law predicts that in order to detect one single ballistic photon (no scattering event over the 5.0 cm distance), the incident number of photons must be $\exp[(5\text{ cm})(100\text{ cm}^{-1})] \approx 10^{217}$. For visible light, 1 J of light has about 10^{18} photons, i.e.,

$$E/(hc/\lambda) = (1\text{ J})/[(6.626 \times 10^{-34}\text{ Js})(3 \times 10^{8}\text{ ms}^{-1})/(0.5 \times 10^{-6}\text{ m})] \approx 2.5 \times 10^{18}\text{ photons}$$

Therefore, the incident light has to be $10^{217}/10^{18} = 10^{199}$ J, which is impossible to deliver.

Quasi-ballistic photon detection might be possible. How many scattering events must quasi-ballistic photons experience in order to yield significant transmission? In order to simplify the question, consider a tissue slab of thickness d with the following optical properties: matched index of refraction with the ambient media, zero absorption coefficient, anisotropy factor $g = 1$. Although this assumption is highly idealized, imaging of real tissues will not be feasible if the imaging of this ideal tissue is not feasible.

If the total incident number of photons is N_{in}, then according to Beer's law, the number of unscattered transmitted photons, N_0, is

$$N_0 = N_{in} \exp(-\mu_t d). \tag{9.39}$$

where $\mu_t = \mu_s$ since absorption is neglected. Let the number of transmitted photons that have experienced i scatterings be denoted by N_i, a real number for this discussion. The values of N_i can be computed (see Appendix A):

$$N_i = N_{in} \exp(-\mu_t d) \frac{(\mu_t d)^i}{i!} = N_0 \frac{(\mu_t d)^i}{i!} \tag{9.40}$$

The sum of all N_i values is equal to N_{in}. Setting albedo $a = 1$, $g = 1$, $N_{in} = 1 \times 10^{18}$, and $\mu_t d = 500$, we solved Eq. (9.39) numerically to illustrate the

Table 9.1. The Number of Scatterings (i) That Occur when N_i Photons are Transmitted[a]

N_i	i	N_i	i	N_i	i
1	319	10^5	347	10^{10}	384
10	324	10^6	354	10^{11}	394
100	330	10^7	361	10^{12}	404
1000	335	10^8	368	10^{13}	416
10,000	341	10^9	376	10^{14}	429

[a] Albedo $a = 1$, $g = 1$, $N_{in} = 1 \times 10^{18}$, and $\mu_t d = 500$.

number of scatterings, i, that occur when N_i photons are transmitted. A few computed i values are listed in Table 9.1. This computation indicates that, on average, 319 scatterings are required to obtain one transmitted photon under the ideal condition of no deflection in photon trajectory. Allowing only a few more scattering events greatly increases the detectable signal, N_i. Therefore, imaging will have to depend on quasi-ballistic photons. The next question is how seriously will anisotropy attenuate these quasi-ballistic photons.

9.5.2. Anisotropy

The anisotropy of scattering, g, is an important factor in imaging. Monte Carlo simulations can illustrate the influence of anisotropy. Consider the propagation of a 1-mJ laser impulse into a tissue. Assume the optical properties are $\mu_a = 0.1\ \text{cm}^{-1}$, $\mu_s = 100\ \text{cm}^{-1}$, $g = 0.9$, $n = 1.37$, and the Monte Carlo z-axis bin size is 10 μm which corresponds to 45 fs. At particular time points, the light distribution is recorded in units of energy density, $U[\text{J/cm}^3]$. All the light at a given depth z is calculated by integration over all r, $U_{1D}(z) = \int U(r, z)\, 2\pi r dr$, to yield one-dimensional energy density, U_{1D}, in units of J/cm per cm^2 of surface area.

Figure 9.7 shows time-resolved Monte Carlo simulations of light propagation after an impulse of radiant exposure. The figures plot the spatial distribution of the one-dimensional energy density, U_{1D}, depicted as a snapshot in time. Several snapshots are depicted in each figure. Figures 9.7a, 9.7b, and 9.7c correspond to simulations where the anisotropy, g, equals 0, 0.90, and 0.99, respectively.

The impulse is attenuated primarily by scattering, leaving behind a trail of scattered photons as it propagates through the tissue. Three dashed lines are indicated: (1) The $\exp(-\mu_t z)$ line represents the total attenuation of ballistic photons. (2) The $\exp(-\mu_p z)$ line represents the attenuation of the primary quasi-ballistic photons comprising the leading edge of the impulse. The number of primary photons which are collected within an array element of finite spatial resolution in the Monte Carlo model depends on the size of the array element used in the simulation. However, in actual experiments the detection device also has an inherent time interval of resolution. Therefore, the definition of primary photons is subject to the time resolution of the simulation or experimental detection device. (3) The $\exp(-\mu_i z)$ line represents the attenuation of those quasi-ballistic photons capable of imaging. Such imaging photons have been arbitrarily specified in this chapter as those photons which will have a total pathlength $L \leq 1.1d$ (where d is the thickness of the tissue) and are approximated by the photons which have penetrated to a depth $z \geq 0.9ct$ for a particular time snapshot. In other words, the imaging photons have only a 10%

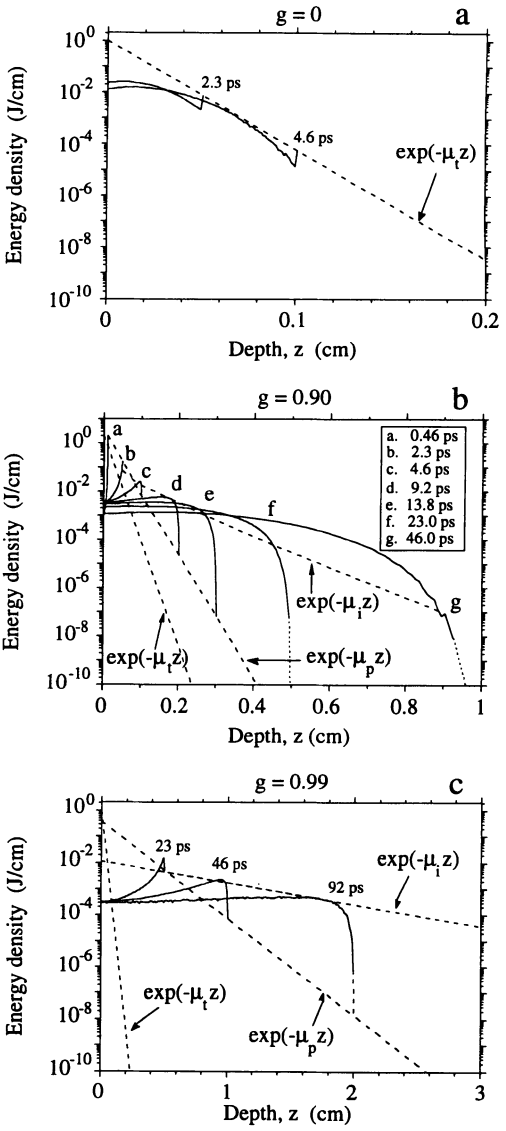

Figure 9.7. Propagation of ballistic, quasi-ballistic, and imaging photons into tissue. Monte Carlo simulations (μ_a = 0.1 cm^{-1}, μ_s = 100 cm^{-1}, g variable) show the depth distribution of photon density (J/cm) for various choices of g at particular time points between 0.46 and 46.0 ps. The dashed lines indicate attenuation curves for ballistic photons, $\exp(-\mu_t z)$, for the primary quasi-ballistic photons comprising the leading edge of the impulse, $\exp(-\mu_p z)$, and for imaging photons which are quasi-ballistic photons which have penetrated at least $z \geq 0.9\ ct$, $\exp(-\mu_i z)$. The dotted lines extend the simulation data that do not appear due to the statistical error of Monte Carlo simulations. (a) For $g = 0$, the attenuation coefficient for all three types of photons are about the same, μ_t. (b) For $g = 0.90$, the attenuation coefficients for ballistic photons, primary photons, and imaging photons are 100, 51, and 8.5 cm^{-1}, respectively. (c) For $g = 0.99$, the attenuation coefficients are 100, 8.5, and 0.019 cm^{-1}, respectively. The penetration of primary and imaging photons increases as the anisotropy increases.

increased total pathlength relative to the ballistic photons. These imaging photons are assumed to be sufficient for useful imaging, but this assumption deserves to be critically questioned in view of the lateral broadening of an impulse seen in Fig. 9.1. The issue of resolution is not addressed in this chapter.

Figure 9.7a shows the propagation for $g = 0$, and the curves (snapshots at $t = z/c$ for $z = 0.05$ cm and 0.1 cm) indicate that $\mu_i \approx \mu_p = \mu_t$ which is 100

cm^{-1} (μ_t is shown). Figure 9.7b shows the propagation for $g = 0.90$, and the three attenuation curves are different: μ_t is 100 cm^{-1}, μ_p is 51 cm^{-1}, and μ_i is 15 cm^{-1}. Figure 9.7c shows the propagation for $g = 0.99$, and the three dashed lines are very different: μ_t is 100 cm^{-1}, μ_p is 8.5 cm^{-1}, and μ_i is 1.8 cm^{-1}. The dashed line $\exp(-\mu_i z)$ extrapolates to a lower initial value (~0.01 J/cm) at zero depth as g increases to 0.99, because the scattering is leaving a trail of photons which are at lower concentration than that for scattering at lower anisotropies. However, the imaging photons are penetrating about 56-fold more readily than the ballistic photons. The net effect is better penetration. The thicknesses of tissue which can be probed with the ballistic vs primary vs imaging photons are related by the ratios of 1:12:56 in a tissue with 0.99 anisotropy. For $g = 0.90$, the ratios are 1:2.0:6.6.

The role of anisotropy can be further appreciated by discussing the attenuation, μ_p, of primary quasi-ballistic photons at the leading edge of the impulse and the attenuation, μ_i, of imaging photons by the descriptions

$$\mu_p = \mu_a + \chi_p \mu_s \tag{9.41}$$

and

$$\mu_i = \mu_a + \chi_i \mu_s \tag{9.42}$$

where χ_p and χ_i are factors between 0 and 1 which reduce the effectiveness of the scattering coefficient. The values of μ_p and μ_i are obtained from Fig. 9.7b for $g = 0.9$. The values of μ_a and μ_s are known. Solving for χ_p and χ_i we obtain

$$\chi_p = \frac{\mu_p - \mu_a}{\mu_s} \tag{9.43}$$

and

$$\chi_i = \frac{\mu_i - \mu_a}{\mu_s} \tag{9.44}$$

For $g = 0.9$, the values of χ_p and χ_i are 0.51 and 0.15, respectively.

To understand how g affects χ, a series of one-dimensional Monte Carlo simulations were conducted with the same optical properties as in Fig. 9.7, however the anisotropy, g, was varied. Two time points, 2.3 and 4.6 ps, were mapped and the leading edge of the impulse at those two time points specified the value of μ_p and hence χ. Figure 9.8 shows the value of χ as a function of g. The dashed line indicates a descriptive relationship between g and χ:

$$\chi \approx \exp[-Ag/(1-g)^m] \tag{9.45}$$

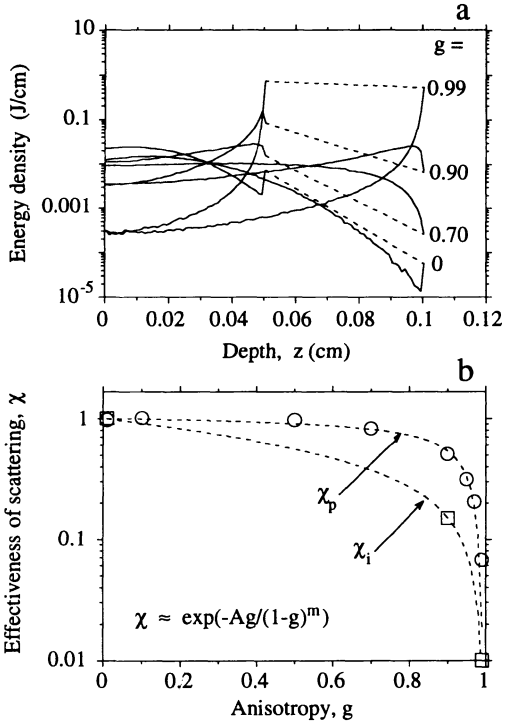

Figure 9.8. The effect of anisotropy on penetration. (a) Monte Carlo simulation, as in Fig. 9.7, for two time points, 0.23 ps and 0.46 ps, for various values of anisotropy, g. (b) The effectiveness of scattering for primary quasi-ballistic photons is defined: $\chi_p = (\mu_p - \mu_a)/\mu_s$. A similar definition is made for the imaging photons: $\chi_i = (\mu_i - \mu_a)/\mu_s$. An empirical relation between χ and g for the two types of photons is shown as dashed lines: $\chi \approx \exp[Ag/(1-g)^m]$, where A and m are 0.119 and 0.764 for χ_p, 0.905 and 0.367 for χ_i. Tissue anisotropies are in the range of 0.8–0.97 and therefore the penetration of primary and imaging photons is greatly affected by the anisotropy. At $g = 0.90$, the relative penetrations of ballistic, primary, and imaging photons are 1:2.0:6.6. At $g = 0.99$, the ratios are 1:12:56.

where A and m are fitted parameters (A and m are 0.119 and 0.764 for χ_p, 0.905 and 0.367 for χ_i). The factors contributing to the values of A and m are not yet fully understood but probably A and m depend on the bin size (or time window) of photon collection. Since actual measurement devices usually involve a finite temporal window of collection, Δt, the pertinence of A and m to measurements is likely to be appropriate. These curves illustrate how anisotropy affects the attenuation of primary and imaging photons. Since tissues are expected to have anisotropies varying in the range of 0.8–0.97, the behavior of χ_p and χ_i versus g becomes important.

ACKNOWLDGEMENT

Computations use the Monte Carlo simulation MCML prepared with the support of the Office of Naval Research, N00015-91-J-1354, and the NIH (R29–HL 45045).

9.6. REFERENCES

1. Jacques SL. "Time resolved propagation of ultrashort laser pulses in turbid tissues," *Appl. Opt.* **28:** 2223–2229 (1989).
2. Cashwell ED, Everett CJ. *A Practical Manual on the Monte Carlo Method for Random Walk Problems*, Pergamon Press, New York (1959).
3. Wang L-H, Jacques SL. *Monte Carlo Modeling of Light Transport in Multi-layered Tissues in Standard C*, University of Texas / M. D. Anderson Cancer Center (1992). The software is available on our anonymous ftp site at laser.mda.uth.tmc.edu (129.106.60.92), or through e-mail to mcml@laser.mda.uth.tmc.edu, or by writing to us at Laser Lab-17, UTMD Anderson Cancer Center, 1515 Holcombe Blvd., Houston, TX 77030.
4. Weinmann JA, Shipley ST. "Effects of multiple scattering on laser pulses transmitted through cloud," *J. Geophys. Res.*, **77:** 7123–7128 (1972).
5. Bucher EA, Lerner RM. "Experiments on light pulse communication and propagation through atmospheric clouds," *Appl. Opt.* **12:** 2401–2414 (1973).
6. Ishimaru A. "Diffusion of a pulse in densely distributed scatterers," *J. Opt. Soc. Am.* **68:** 1045–1050 (1978).
7. Shimizu K, Ishimaru A, Reynolds L, Breuckner AP. "Backscattering of a picosecond pulse from densely distributed scatterers," *Appl. Opt.* **18:** 3484–3488 (1979).
8. Kuga Y, Ishimaru A, Bruchner AP. "Experiments on picosecond pulse propagation in a diffuse medium," *J. Opt. Soc. Am.* **73:** 1812–1815 (1983).
9. Ito S, Furutsu K. "Theory of light pulse propagation through thick clouds," *J. Opt. Soc. Am.* **70:** 366–374 (1980).
10. Patterson MS, Chance B, Wilson BC. "Time resolved reflectance and transmittance for the noninvasive measurement of tissue optical properties," *Appl. Opt.* **28:** 2331–2336 (1989).
11. Madsen SJ, Wilson BC, Patterson MS, Park YD, Jacques SL, Hefetz Y. "Experimental tests of a simple diffusion model for the estimation of scattering and absorption coefficients of turbid media from time-resolved diffuse reflectance measurements," *Appl. Opt.* **31:** 3509–3517 (1992).
12. Bonner RF, Nossal R, Weiss GH. "A random walk theory of time-resolved optical absorption spectroscopy in tissue," in Chance B (ed.), *Proc. Workshop Photon Migration in Tissues*, Plenum Press, New York (1989).
13. Nossal R, Bonner RF, Weiss GH. "The influence of pathlength on remote optical sensing of properties of biological tissues," *Appl. Opt.* **28:** 2238–2244 (1989).
14. Duderstadt JJ, Hamilton LJ. *Nuclear Reactor Analysis*, Wiley, New York (1976).
15. Jacques SL, Hielscher AH, Wang LH. "Effects of sources, boundaries, and heterogeneities on photon migration," in Alfano RR (ed.), *Proceedings on Advances in Optical Imaging and Photon Migration*, Optical Society of America Vol. 21, pp. 83–87 (1994).
16. Tromberg BJ, Svaasand LO, Tsay TT, Haskell RC. "Properties of photon density waves in multiple-scattering media," *Appl. Opt.* **32:** 607–616 (1993).
17. Hielscher AH, Tittel FK, Jacques SL. "Non invasive monitoring of blood oxygenation by phase

resolved transmission spectorscopy," in Chance B, Alfano RR (eds.), *Photon Migration and Imaging in Random Media and Tissues*, Proc. SPIE Vol. 1888 pp. 275–288 (1993).
18. Piston DW, Marriott G, Radivoyevich T, Clegg RM, Jovin TM, Gratton E. "Wide-band acousto-optic light modulator for frequency domain fluorometry and phosphorimetry," *Rev. Sci. Instrum.* **60:** 2596–2600 (1989).
19. Peterman K. *Laser Diode Modulation and Noise*, KTK Scientific Publishers, Dodrecht (1988).
20. Lakowicz JR, Laczko G, Gryczynski I. "2-GHz frequency-domain fluorometer," *Rev. Sci. Instrum.* **57:** 2499–2506 (1986).
21. Press WH, Flannery BP, Teukolsky SA, Vetterling WT. *Numerical Recipes in C*, 2nd ed., New York, Cambridge University Press (1992).
22. Jacques SL. "Time-resolved reflectance spectroscopy in turbid tissues," *IEEE Trans. Biomed. Eng.* **36:** 1155–1161 (1989).
23. Jacques SL, Flock ST. "Effect of surface boundary on time-resolved reflectance: measurements with a prototype endoscopic catheter," in Chance B (ed.), *Proceedings of Time-Resolved Spectroscopy and Imaging of Tissues*, SPIE Vol. 1431, pp. 12–20 (1991).
24. Wray S, Cope M, Delpy DT, Wyatt JS, Reynolds EOR. "Characterization of the near infrared absorption spectra of cytochrome aa_3 and haemoglobin for the non-invasive monitoring of cerebral oxygenation," *Biochim. Biophys. Acta* **933:** 184–192 (1988).
25. Sevick EM, Chance B, Leigh J, Nioka S, Maris M. "Quantitation of time- and frequency-resolved optical spectra for the determination of tissue oxygenation," *Anal. Biochem.* **195:** 330–351 (1991).
26. Hielscher AH, Liu H, Wang LH, Tittel FK, Chance B, Jacques SL. "Determination of blood oxygenation in the brain by time-resolved reflectance spectroscopy (I): Influence of the skin, skull and meniges," in Chance B, Alfano RR (eds.), *Biochemical Diagnostic Instrumentation A: Optical Diagnosis of Blood and Blood Components*, Proc. SPIE Vol. 2136, pp. 4–15 (1994).
27. Liu H, Hielscher AH, Beauvoit B, Wang LH, Jacques SL, Tittel FK, Chance B. "Determination of blood oxygenation in the brain by time-resolved reflectance spectroscopy (II): Contribution of vascular absorption and tissue background absorption," in Chance B, Alfano RR (eds.), *Biochemical Diagnostic Instrumentation A: Optical Diagnosis of Blood and Blood Components*, Proc. SPIE Vol. 2136, pp. 16–25 (1994).

9.7. APPENDIX

The proof of Eq. (9.39) is presented in this appendix. Consider a tissue slab of thickness d. The tissue optical properties are: matched refractive index with the ambient media, total interaction coefficient μ_t, ideal albedo $a = 1$, and ideal anisotropy $g = 1$. An infinitely narrow photon beam is incident perpendicularly upon the tissue along the z axis, where the z axis is perpendicular to the tissue surface and originates on the tissue surface. Let us define $P_i\{z_1, z_2\}$ as the probability of a photon traveling from z_1 to z_2 in the ideal tissue with i scatterings. Equation (9.39) is equivalent to

$$P_i\{0, d\} = \exp(-\mu_t d) \frac{(\mu_t d)^i}{i!} \tag{9.A1}$$

where $i = 0, 1, 2, \ldots$. Induction will be used to prove Eq. (9.A1). First, we will prove for $i = 0$. According to Beer's law,

$$P_0\{0, d\} = \exp(-\mu_t d) = \exp(-\mu_t d)\,(\mu_t d)^0 / 0! \tag{9.A2}$$

where both $(\mu_t d)^0$ and 0! are unity. Therefore, Eq. (9.A1) is valid for $i = 0$. Second, we will prove if Eq. (9.A1) is correct for $i = j$, i.e.,

$$P_j\{0, d\} = \exp(-\mu_t d)\,\frac{(\mu_t d)^j}{j!} \tag{9.A3}$$

then Eq. (9.A1) is correct for $i = j + 1$.

The probability of no interactions between 0 and z is

$$P_0\{0, z\} = \exp(-\mu_t z) \tag{9.A4}$$

which is Beer's law or Eq. (9.A1) for $i = 0$. According to the definition of the total interaction coefficient (equal to the scattering coefficient, since $a = 1$), the probability of one interaction between z and $z + \Delta z$ is

$$P_1\{z, z + \Delta z\} = \mu_t \Delta z \tag{9.A5}$$

ignoring the probability of two or more interactions, where Δz is a small finite increment of z. The probability of j interactions between $z + \Delta z$ and d is $P_j\{z + \Delta z, d\}$, which can be expanded to the zero order with a first-order error term, i.e.,

$$P_j\{z + \Delta z, d\} = P_j\{z, d\} + P_j'\{z + k\Delta z, d\}\,\Delta z \tag{9.A6}$$

where k is a constant between 0 and 1, and $P_j'\{z + k\Delta z, d\}$ is a first derivative with respect to z. Consequently, the probability that photons experience no interactions between 0 and z, one interaction between z and $z + \Delta z$, and j interactions between $z + \Delta z$ and d is

$$\begin{aligned} P_0\{0, z\}\, P_1\{z, z + \Delta z\}\, P_j\{z + \Delta z, d\} \\ &= \exp(-\mu_t z)\,(\mu_t \Delta z)\,[P_j\{z, d\} + P_j'\{z + k\Delta z, d\}\,\Delta z] \\ &= \exp(-\mu_t z)\,(\mu_t \Delta z)\,[P_j\{z, d\} + P_j'\{z + k\Delta z, d\}\,\Delta z^2] \end{aligned} \tag{9.A7}$$

In Eq. (9.A7), letting $\Delta z \to 0$, replacing Δz with dz, and ignoring the second-order infinitesimal term, one obtains

$$P_0\{0, z\}\, P_1\{z, z + \Delta z\}\, P_j\{z + \Delta z, d\} \rightarrow \exp(-\mu_t z)\, \mu t\, P_j\{z, d\}\, dz$$

$$= \exp(-\mu_t z)\, \mu_t \exp[-\mu_t (d - z)] \frac{[\mu_t (d - z)]^j}{j!} dz$$

$$= \exp(-\mu_t d) \frac{\mu_t^{j+1}}{j!} (d - z)^j\, dz \tag{9.A8}$$

where $P_j\{z, d\}$ is substituted by Eq. (9.A3) in which d is replaced with $d - z$. The integration of Eq. (9.A8) over the full depth covers all cases of $j + 1$ interactions, i.e.,

$$P_{j+1}\{0, d\} = \int_0^d \exp(-\mu_t d) \frac{\mu_t^{j+1}}{j!} (d - z)^j\, dz$$

$$= \exp(-\mu_t d) \frac{\mu_t^{j+1}}{j!} \int_0^d (d - z)^j\, dz$$

$$= \exp(-\mu_t d) \frac{(\mu_t d)^{j+1}}{(j + 1)!} \tag{9.A9}$$

Equation (9.A9) means Eq. (9.A1) is valid for $i = j + 1$. Therefore, Eq. (9.A1) is valid for all i values based on this induction.

Since all incident photons will transmit the ideal tissue, the sum of all $P_i\{0, d\}$ should be 1, i.e.,

$$\sum_{i=0}^{\infty} P_i\{0, d\} = \sum_{i=0}^{\infty} \exp(-\mu_t d) \frac{(\mu_t d)^i}{i!}$$

$$= \exp(-\mu_t d) \sum_{i=0}^{\infty} \frac{(\mu_t d)^i}{i} \tag{9.A10}$$

$$= \exp(-\mu_t d) \exp(\mu_t d) = 1$$

When $i = 0$, Eq. (9.A1) simply reduces to Beer's law. When $i = 1$, Eq. (9.A1) becomes

$$P_1\{0, d\} = \exp(-\mu_t d)\, \mu_t d \tag{9.A11}$$

When "$\mu_t d$" is small (an optically thin slab), the exponential term can be expanded to the zero order and Eq. (9.A11) becomes

$$P_1\{0, d\} = \mu_t d \tag{9.A12}$$

which is essentially Eq. (9.A5), except that the slab thickness is d instead of Δz.